processes

MDPI

Article

Enhancing Oxygen Permeation via the Incorporation of Silver Inside Perovskite Oxide Membranes

Teng Ma [1], Ning Han [2], Bo Meng [1], Naitao Yang [1], Zhonghua Zhu [3] and Shaomin Liu [2,*]

[1] School of Chemical Engineering, Shandong University of Technology, Zibo 255049, China; 18369956561@163.com (T.M.); mb1963@126.com (B.M.); naitaoyang@126.com (N.Y.)
[2] Department of Chemical Engineering, Curtin University, Perth, WA 6102, Australia; ning.han@curtin.edu.au
[3] School of Chemical Engineering, The University of Queensland, Brisbane 4072, Australia; z.zhu@uq.edu.au
* Correspondence: shaomin.liu@curtin.edu.au; Tel.: +61-8-92669056

Received: 11 February 2019; Accepted: 3 April 2019; Published: 8 April 2019

Abstract: As a possible novel cost-effective method for oxygen production from air separation, ion-conducting ceramic membranes are becoming a hot research topic due to their potentials in clean energy and environmental processes. Oxygen separation via these ion-conducting membranes is completed via the bulk diffusion and surface reactions with a typical example of perovskite oxide membranes. To improve the membrane performance, silver (Ag) deposition on the membrane surface as the catalyst is a good strategy. However, the conventional silver coating method has the problem of particle aggregation, which severely lowers the catalytic efficiency. In this work, the perovskite oxide $La_{0.8}Ca_{0.2}Fe_{0.94}O_{3-a}$ (LCF) and silver (5% by mole) composite (LCFA) as the membrane starting material was synthesized using one-pot method via the wet complexation where the metal and silver elements were sourced from their respective nitrate salts. LCFA hollow fiber membrane was prepared and comparatively investigated for air separation together with pure LCF hollow fiber membrane. Operated from 800 to 950 °C under sweep gas mode, the pure LCF membrane displayed the fluxes from 0.04 to 0.54 mL min^{-1} cm^{-2}. Compared to pure LCF, under similar operating conditions, the flux of LCFA membrane was improved by 160%.

Keywords: mixed conducting; ceramic membranes; perovskite oxides; air separation

1. Introduction

Cost-effective oxygen production from air separation is important for industrial and environmental processes as oxygen plays a vital role in improving the combustion efficiency for steel industry and clean energy projects with CO_2 management. Carbon capture and storage has been recognized as the most realistic technology to help the climate change by preventing the release of large quantities of CO_2 into the atmosphere from large point sources like coal power plants. However, the prerequisite for this achievement is to get the highly purified CO_2 in a very economic manner as the waste gas from these power plants using air as the oxidant only contain 12–15% CO_2. If pure oxygen instead of air is used during the combustion process for industries, the major constituent of the waste gas produced would be highly purified CO_2, which can be easily captured for subsequent storage. In this circumstance, the economics for clean energy projects is closely correlated with the oxygen production. Current large scale O_2 production by conventional cryogenic process or pressure adsorption methods is expensive and energy intensive. Ceramic membranes with mixed ionic and electronic conducting (MIEC) properties can deliver 100% pure O_2 under the differential O_2 concentration gradient at high temperatures, offering the potential to improve the economics of many industrial processes with carbon mitigation [1–15]. These MIEC membranes also have applications as membrane reactors for many important oxidative reactions to improve the product

selectivity (if controlled by the reaction equilibrium) or purity without including nitrogen in the product system [16–26]. However, such advanced applications require the membranes to possess strong stability against some gases like NO_x, CO_2, H_2, or hydrocarbons [27–31].

Many previous works in MIEC membranes employed the perovskite compositions of ABO_3 based on these doped $SrCoO_3$ including $SrCo_{0.8}Fe_{0.2}O_{3-\delta}$, $SrCo_{0.9}Sc_{0.1}O_{3-\delta}$, $Ba_{0.5}Sr_{0.5}Co_{0.8}Fe_{0.2}O_{3-\delta}$, and $La_{0.6}Sr_{0.4}Co_{0.2}Fe_{0.8}O_{3-\delta}$ [31–38]. These highly permeable membranes can only be applied for pure oxygen production purpose using mild gas atmosphere under the oxygen gradient of air (high pressure)/oxygen (1 atm). In the presence of acidic gas of CO_2 and reducing gases like H_2 or CH_4, these Sr- or Co-containing perovskite membranes would have a very low O_2 flux and poor membrane stability due to the reaction between these gases and the membrane materials [39]. One typical example is $Ba_{0.5}Sr_{0.5}Co_{0.8}Fe_{0.2}O_{3-\delta}$ (BSCF) [36]. For the hollow fiber membrane with wall thickness of 0.25 cm, under air/helium gradient and at 850 °C, the oxygen flux is 2.20 mL min^{-1} cm^{-2}; however, the flux would be reduced to zero once the sweep gas was switched to CO_2 due to the high basicity of Ba and Sr, causing a fast carbonate formation on the membrane surfaces [41]. One strategy to overcome poor stability is to tailor the ABO_3 composition with less CO_2-sensitive elements like La and Ca and without cobalt [25,40,41]. For example, $BaCe_xFe_{1-x}O_{3-\delta}$ (BCF) displayed a higher stability even in H_2-containing atmosphere [42].

In particular, Price et al. verified the chemical stability of $La_{1-x}Ca_xFe_xO_{3-\delta}$ perovskites in reducing environments for the syngas production from methane partial oxidation at high temperatures [43]. Reviewing the performances of all these perovskite membranes from materials perspective, there exists a trade-off phenomenon between the stability and oxygen flux with improvement in one property but always to the detriment of the other property. One way to solve this dilemma is to improve the performance from engineering considerations based on these cobalt-free perovskite oxide membranes. As oxygen permeation through these MIEC membranes involves surface oxygen exchange reactions and ionic bulk diffusion, oxygen flux can be further improved via coating the catalyst on the surface or a thin membrane technology. Palladium and platinum have been successfully applied as catalysts to improve O_2 fluxes of perovskite membranes [44,45]. Silver (Ag) is a promising alternative to Pt or Pd-based catalyst due to its affordable price, good oxygen solubility, and compatible catalytic activity to promote the overall oxygen permeation rate [46–48]. For example, Tan et al. used a brush-painting method to coat the $La_{0.6}Sr_{0.4}Co_{0.2}Fe_{0.8}O_{3-\delta}$ (LSCF) membranes with flux improvement by a factor up to 10 depending on the operating conditions [46]. However, due to the lower melting point, the Ag particles are easily aggregated during the high-temperature operation and gradually lose the catalytic effect [46].

Here, we report a novel silver–perovskite oxide composite hollow fiber membrane with a composition of $La_{0.8}Ca_{0.2}Fe_{0.94}O_{3-a}$ + 0.05 Ag (LCFA) for efficient oxygen separation. The perovskite oxides and silver composite were synthesized from one-pot method via the combined ethylene glycol (EG) and citric acid (CA) complexation. In this method, EG and CA were used as the chelating reagent to stabilize the four metal (La, Ca, Fe, and Ag) ions from their respective nitrate salts. The complex solution was thickened and further heat-treated to form the final perovskite oxides with Ag particles around 2.5% (by weight) uniformly distributed among the $La_{0.8}Ca_{0.2}Fe_{0.94}O_{3-a}$ (LCF) grains or particles. LCF hollow fiber membrane was chosen for demonstration because of the well-known stability of LCF and favorable membrane geometry providing a larger membrane area per unit volume.

2. Experimental

2.1. Preparation of LCF/LCFA Powders and Hollow Fibre Membranes

$La_{0.8}Ca_{0.2}Fe_{0.94}O_{3-\delta}$ + 0.05 Ag (2.4% by weight) (LCFA) perovskite oxides and silver composite powder were synthesized using a one-pot complexation method. A stoichiometric amount of citric acid, ethylene glycol, $La(NO_3)_3{\cdot}6H_2O$ (purity 99%, Sinopharm Chemical Reagent Co., Ltd., Beijing, China),

$Ca(NO_3)_2{\cdot}4H_2O$ (purity 99%, Sinopharm Chemical Reagent Co., Ltd., Beijing, China), $Fe(NO_3)_3{\cdot}9H_2O$ (purity 98.5%, Badische Anilin-und-Soda-Fabrik, Shandong, China), and $AgNO_3$ (purity 99.8%,Tianjin Tiangan chemical technology Development Co., Ltd., Tianjin, China) were dissolved in the de-ionized water to form an aqueous solution with the final mole ratio of CA:EG:metal ions of 1.2:1.2:1 [49]. In order to form a transparent solution without unfavorable salt precipitation, the pH value was adjusted to 8 using nitric acid (HNO_3, Sinopharm Chemical Reagent Co., Ltd., Beijing, China) or ammonia ($NH_3{\cdot}H_2O$ Sinopharm Chemical Reagent Co., Ltd., Beijing, China). Then, the aqueous solution was heated at 80 to 100 °C under a continuous stirring condition to achieve a viscous gel. The gel was further dried inside an oven at 200 °C to form a black powder. The synthesized LCFA powder was subsequently calcined at 900 °C for 4 hours to remove the residual carbon and obtain composite powder. For hollow fiber synthesis, the calcined LCFA powder was ground and milled in ethanol (18 wt %) within a planetary mill for 48 hours followed by sieving through a 200-mesh sifter to rule out larger particles.

LCFA hollow fiber precursors were prepared using the sieved powder via the phase inversion and sintering method [50]. The spinning mixture was prepared by dispersing LCFA powder into the polymer solution of poly(ether sulfones) (PESF):n-methyl-2-pyrrolidone (NMP):LCFA (1:4:8 by weight ratio). The mixture was stirred for 48 h and degassed prior to spinning. Home-made spinneret with an orifice diameter/inner diameter of 3.0/1.2 mm was used for extrusion of the hollow fiber precursor, where de-ionized water was used as the internal coagulant while tap water was used as the external coagulant [51]. After drying, the hollow fiber precursors were sintered at 1250 °C for 4 h to obtain dense perovskite and Ag composite (LCFA) hollow fibers. In a similar procedure, LCF hollow fiber membrane was prepared. All membranes were subjected to nitrogen permeation test to ensure their gas-tightness [52].

2.2. Oxygen Permeation Measurement

Nitrogen permeation test was used to evaluate the gas-tightness of LCF/LCFA hollow fibers as detailed elsewhere [52]. Only these hollow fibers with gas-tightness (less than 1×10^{-8} mol m^{-2} Pa^{-1} s^{-1}) were chosen to perform the oxygen permeation tests. Oxygen permeation fluxes of LCFA and the original LCF hollow fibers were quantified using the custom-made permeation test module described elsewhere [51]. Air was fed (flow rate 100 mL/min) into the shell side of the test module while helium was passed through the hollow fiber lumen side to collect the permeated oxygen. The composition of the permeate gas stream was analyzed using a gas chromatograph (Agilent 6890N, Santa Clara, CA, US) equipped with a 5 Å molecular sieve column and a thermal conductivity detector (TCD). The detailed calculation of the oxygen flux was described previously [33].

2.3. Characterization

Crystal structure of LCFA hollow fibers and the powders were characterized by powder X-ray diffraction (XRD, Bruker D8 Advance, Berlin, Germany) using a Cu-K radiation. A continuous scan mode was used to collect patterns at 2θ range of 20° to 80° using a 0.02° step size and a 0.01 s step time. The X-ray tube potential and current were set at 40 kV and 30 mA, respectively. The morphologies of the hollow fibers were detected using scanning electron microscope (SEM, FEI Sirion 200, Amsterdam, Netherlands). Gold sputtering was performed on the surface of the fibers prior to the SEM observation. The sub-micron structure of the hollow fiber and the powders were also probed using transmission electron microscope (TEM, JEOL EM-2100, Tokyo, Japan). The elemental maps were obtained by energy dispersive X-ray spectroscopy using the Super-X detector on the Titan with a probe size of 1 nm and a probe current of 0.4 nA. Thermal expansion behaviors of LCF and LCFA powders were probed using dilatometry (DIL, 402C, Netzsch, Germany) with a heating rate of 5 °C min^{-1} from room temperature to 1400 °C. LCF and LCFA powders were pressed into rectangular bars prior to the dilatometry tests [53].

3. Results and Discussion

3.1. Phase Structure and Thermal Shrinkage Behavior of LCF and LCFA

Figure 1 exhibits one typical TEM with the corresponding EDS elemental mapping and spectra of LCFA composite powder prepared at 900 °C. As can be seen from Figure 1a,b, the elements of La, Ca, Fe, O, and Ag are uniformly distributed in the composite particles with size around 100 nm. From the SEM image in Figure 1c, it is clear that the sintered powder is always agglomerated by these smaller particles. However, the presence of a very large agglomerate is unfavorable to the subsequent preparation of gastight perovskite hollow fiber membranes; thus, the sintered LCFA or LCF powder was further processed by milling and sieving to eliminate larger particles. Figure 2 depicts the room temperature X-ray diffraction patterns of the LCF and LCFA powder prepared at 900 °C from their complexing precursors. These powders were applied as the starting membrane material for hollow fibers. As can be seen from Figure 2a, LCF has a single-phase perovskite with cubic structure as evidenced by the characteristic diffraction peaks at 2θ of 22.92°, 32.51°, 40.16°, 46.98°, 53.24°, 58.06°, 60.08°, 72.96°, and 77.8°. By contrast, in addition to the major cubic perovskite phase, there are extra peaks at 2θ of 38.19° and 44.91°, which belong to the characteristic peaks (higher magnification in Figure 2b) of Ag metal phase. Noteworthy is that some unknown phases were detected at 2θ around 25°, 53°, and 54°. The crystal phase of LCFA was further studied in air and nitrogen using high-temperature X-ray diffraction (HT-XRD), with the result shown in Figure 2c. The comparison of these XRD patterns in room and high temperatures indicates that both the cubic perovskite phase and Ag metal phase are very stable without phase transition occurring despite the temperature alteration from room temperature to 900 °C and gas atmosphere change from air to nitrogen. Good phase stability is an excellent feature for LCFA to be applied as the membrane material, as the phase transition with the temperature change would induce stress possibly breaking the membrane [54]. Another parameter influencing the membrane's physical integrity is its thermal shrinking/expansion behavior with the temperature change. The measured thermal expansion coefficients (TECs) (Figure 2d) of LCF and LCFA bar samples sintered at 1400 °C were 11.59 $\times$ 10^{-6} K^{-1} and 11.55 $\times$ 10^{-6} K^{-1}, respectively, much smaller than other perovskite oxides of BSCF (24 $\times$ 10^{-6} K^{-1}) [55], $BCFSn_{0.1}$ (15.1 $\times$ 10^{-6} K^{-1}) [56], and LSC (15.9 $\times$ 10^{-6} K^{-1}) [53]. Ceramic membranes with smaller TEC values could also reduce the thermal stress during the heating–cooling cycling operation, helpful to maintain the membrane integrity.

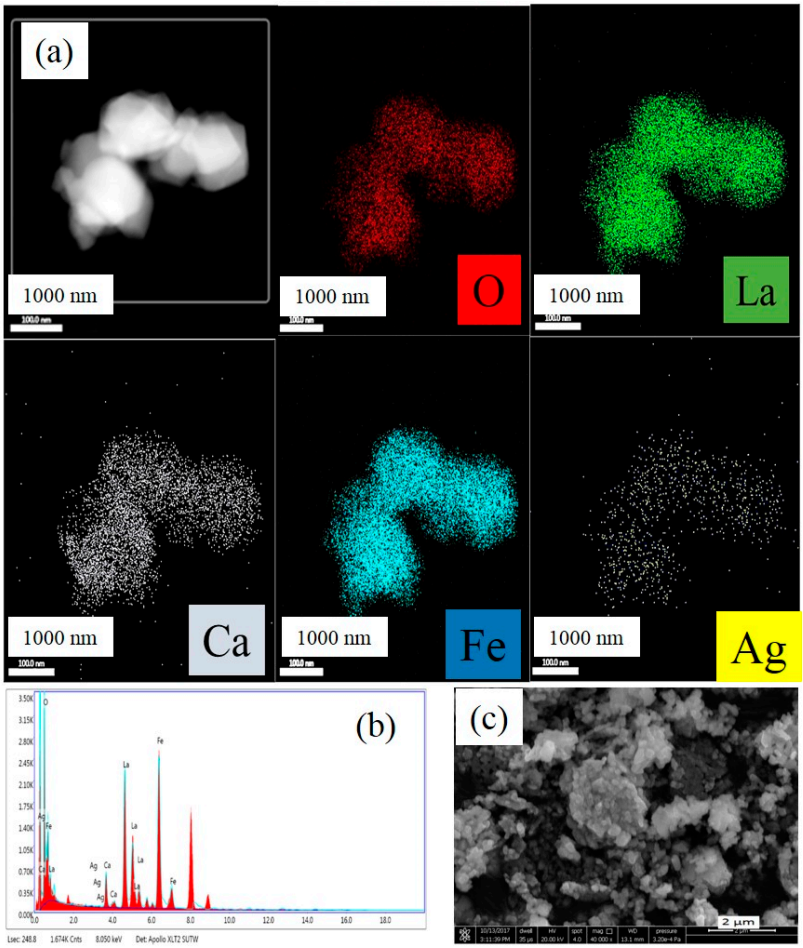

Figure 1. Typical TEM (**a**) and EDS elemental mapping and EDS spectra (**b**) and SEM image (**c**) of $La_{0.8}Ca_{0.2}Fe_{0.94}O_{3-\delta}$ + 0.05 Ag (LCFA) composite powder prepared by the EDTA–citric acid method (calcined at 900 °C).

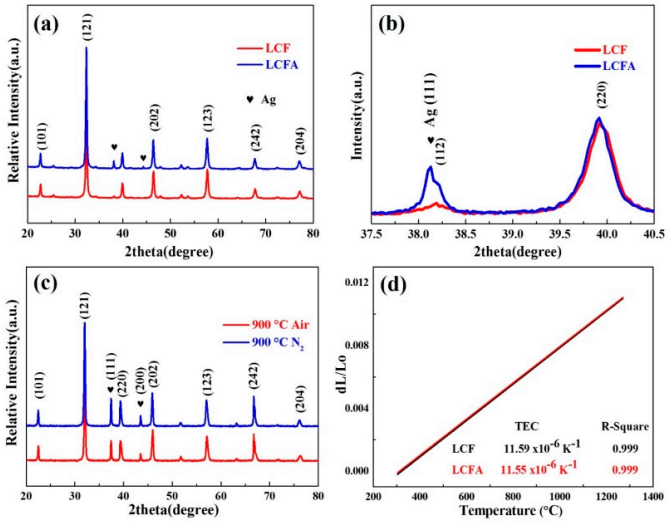

Figure 2. (**a**–**c**) The powder X-ray diffraction (XRD) patterns of $La_{0.8}Ca_{0.2}Fe_{0.94}O_{3-a}$ (LCF) and LCFA. (**a**) Room temperature; (**b**) the magnified characteristic peaks of metallic Ag; (**c**) high temperature at 900 °C in air or nitrogen of LCFA; and thermal expansion profiles (**d**) of the LCF and LCFA bar samples sintered at 1400 °C from dilatometry (heating rate: 5 °C min^{-1}).

3.2. Morphology of LCF and LCFA Hollow Fiber Membranes

Figure 3 displays SEM images of the prepared LCF (Figure 3a–c) and LCFA (Figure 3d–f) hollow fiber membranes sintered at 1250 °C with complete gas-tightness to block the mass transport in molecular diffusion. Both of the hollow fiber membranes have the fiber wall thickness around 0.2 mm (Figure 3a,d). However, the real densified separating layer for ionic diffusion has a thickness much less than the overall fiber wall thickness due to the presence of micro-sized pores. Such an asymmetric structure was derived from the polymer phase inversion process, the reason of which had been described previously [57]. Figure 3b–f exhibit the fiber surface views with a clearly visible grain size from 0.2 to 0.8 microns and from 0.3 to 1.5 microns for LCF and LCFA, respectively. The grain size has a significant influence on the permeation behavior of the membrane [58]. The larger grain size of LCFA than LCF is due to the introduction of Ag, which was playing the role of sintering aid to facilitate the LCF particle densification. Further inspection of these SEM images from two surface views exhibited that due to the less densification of LCF, many pores were still observed in LCF surface; by contrast, a more densified surface morphology was achieved on LCFA membrane. Noteworthy that despite the existence of micro-pores in Figure 3b,c, there are isolated pores without a connected porosity; thus, the LCF membrane still has the required gas-tightness for oxygen permeation. Figure 4 displays one typical TEM from the crushed LCFA hollow fiber with the corresponding EDS elemental mapping and spectra. Despite that the LCFA hollow fiber was sintered at 1250 °C, silver was still unfirmed presented inside the membrane evidenced by the mapping results and spectra mirroring the thermal stability of Ag inside the composite. The presence of Ag in 2.5 wt % of LCFA does not have much impact on the mechanical strength. The measured three-point bending strength of the LCF or LCFA hollow fiber is around 310 MPa. In practical application, ceramic hollow fiber should have sufficiently high mechanical strength, particularly when long hollow fiber modules are being applied. Low mechanical strength is generally the limiting factor towards its large scale application. In case of LCF or LCFA hollow fiber, its mechanical strength is the best among the various perovskite oxide hollow fibers tested, for example, almost 3 and 5 times than that measured for $La_{0.6}Sr_{0.4}Co_{0.2}Fe_{0.8}O_{3-\delta}$ (LSCF) and $SrCe_{0.95}Yb_{0.05}O_{2.975}$, respectively [39,59].

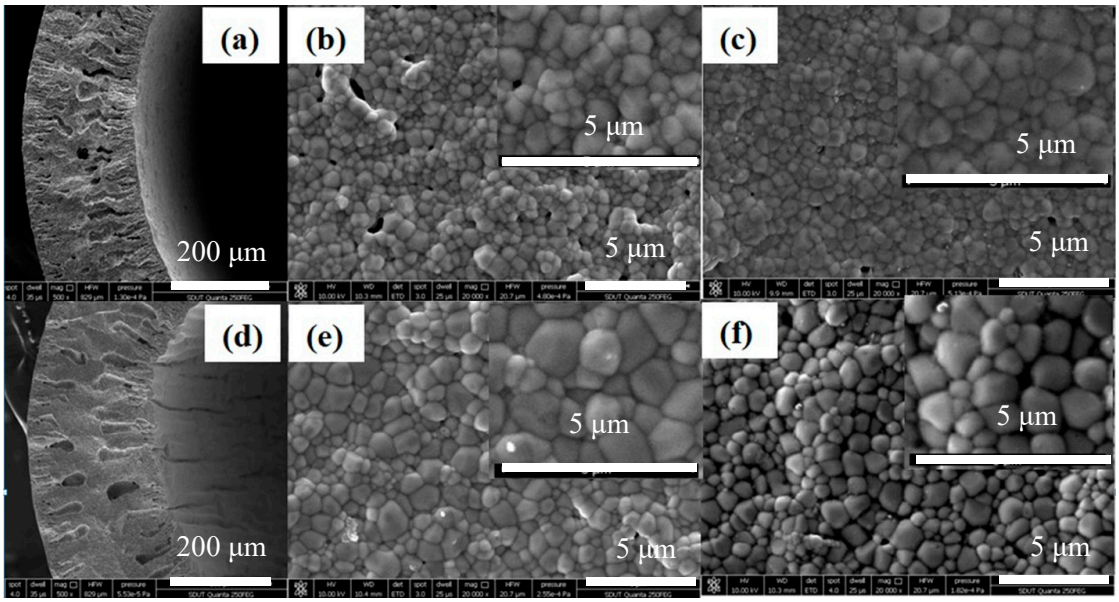

Figure 3. Typical SEM images of LCF and LCFA hollow fiber membranes (**a**–**c**) LCF; (**d**–**f**) LCFA; (**a**,**d**) cross section of fiber wall; (**b**,**e**) inner surface; (**c**,**f**) external surface (inset of (**b**,**c**,**e**,**f**) higher magnification; all magnification bar size at 5 microns).

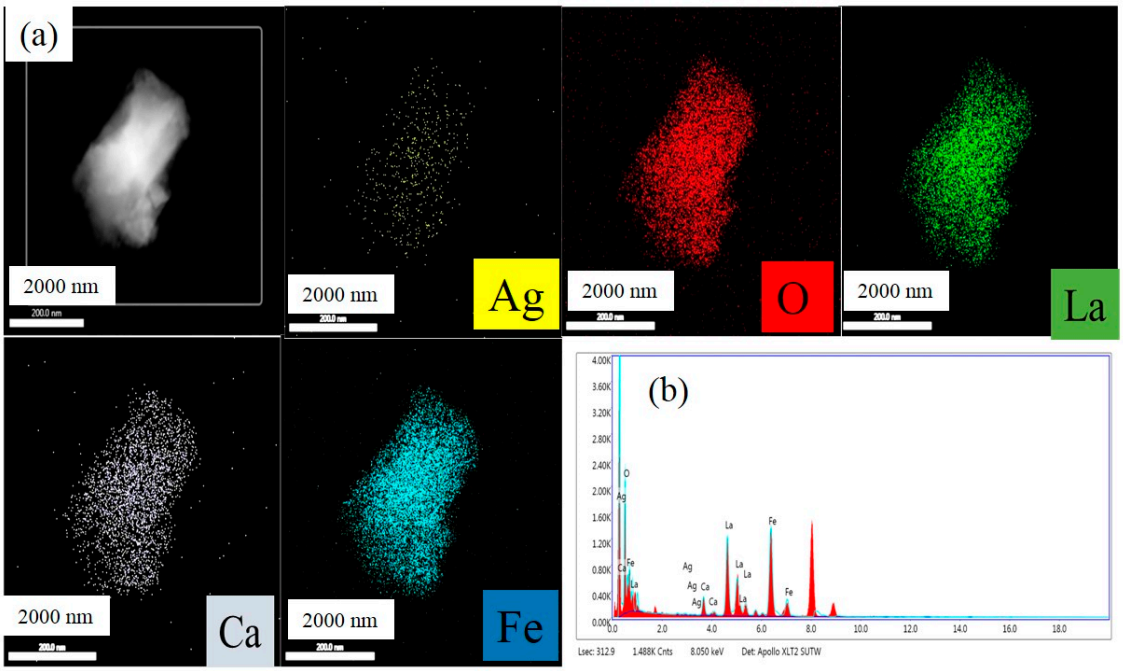

Figure 4. Typical TEM (**a**) and EDS elemental mapping and EDS spectra (**b**) of the LCFA powder crushed from LCFA hollow fiber membrane (sintered at 1250 °C; all magnification bar size at 100 nm).

3.3. Oxygen Permeation Test

Oxygen permeation was tested using air as the feed gas and helium as the sweep gas at high temperatures. Hollow fiber external surface was exposed directly to air flow and helium sweeping gas was passed through the lumen. Driven by the oxygen partial pressure (0.21 atm) gradient across the membrane, oxygen would be permeated from air side to the lumen. The oxygen fluxes of three types of hollow fibers of LCF and LCFA as functions of helium sweep gas flow rate from 30 to 180 mL min^{-1} and temperatures between 800 and 950 °C are displayed in Figure 5. Figure 5a shows the oxygen flux of LCF, which increased notably with temperature. For instance, at a helium sweeping rate of 30.0 mL min^{-1}, the oxygen flux rose from 0.04 to 0.09, 0.29, and 0.54 mL min^{-1} cm^{-2} as the temperature increased from 800 to 850, 900, and 950 °C, respectively. Such flux enhancement with temperature rise is due to the improved oxygen surface exchange reaction rate and oxygen ion bulk-diffusion rate at higher operation temperatures [10]. When the operation temperature is lower than 800 °C, the oxygen flux is too low to be accurately measured. Figure 5a also displays the impact of sweep gas rate on the flux value. The influence from sweep gas rate is more complex than the temperature. When the sweep gas flow rate is increased, the oxygen partial pressure at the permeate side is decreased thus increasing the driving force for oxygen permeation, which has the trend to improve the oxygen flux value. On the other hand, a lower oxygen partial pressure in the permeate side decreases the surface oxygen exchange reaction kinetics or increases the surface oxygen exchange resistance [37,60,61]. In theory, at a certain temperature, with the enlargement of sweep gas flow rate or the decrease of oxygen partial pressure in the permeate side, the oxygen flux value would experience three stages: firstly increased (Stage-I), then saturated (Stage-II), and finally decreased (Stage-III) [10,37,60,61]. When looking at the Figure 5a, the phenomena of these three stages are clearly observed. Figure 5a also compares the oxygen flux values of two kinds of LCF hollow fiber membranes from $(La_{0.8}Ca_{0.2})_{1.01}FeO_{3-\delta}$ (1% A-site cation surplus in ABO_3 from literature measured at 950 °C) and $La_{0.8}Ca_{0.2}Fe_{0.94}O_{3-\delta}$ (6% B site cation deficiency) operated at relatively similar conditions [41]. Apparently, the latter composition has a larger flux than the former as more oxygen vacancies were created by the B-site cation deficiency. Further inspection of Figure 5, LCFA (Figure 5b) displays the best oxygen fluxes compared to LCF (Figure 5a). For example, at 900 °C and swept by 90 mL min^{-1},

the flux values of LCF and LCFA were 0.28 and 0.73 mL min^{-1} cm^{-2}, respectively. Compared to LCF, the flux by LCFA had been improved by 160%, respectively. Figure 5c shows Arrhenius plots of oxygen permeation fluxes through two hollow fiber samples of LCF and LCFA. Applying the Arrhenius equation, activation energies for oxygen transport through fibers under the conditions of Figure 5a,b are 196.07 (Figure 5a) and 134.87 (Figure 5b). Apparently, LCFA (Figure 5b) has the lowest activation energy resulting in a better oxygen permeation rate. The reason for the better oxygen flux value from LCFA membrane can be schematically shown in Figure 6.

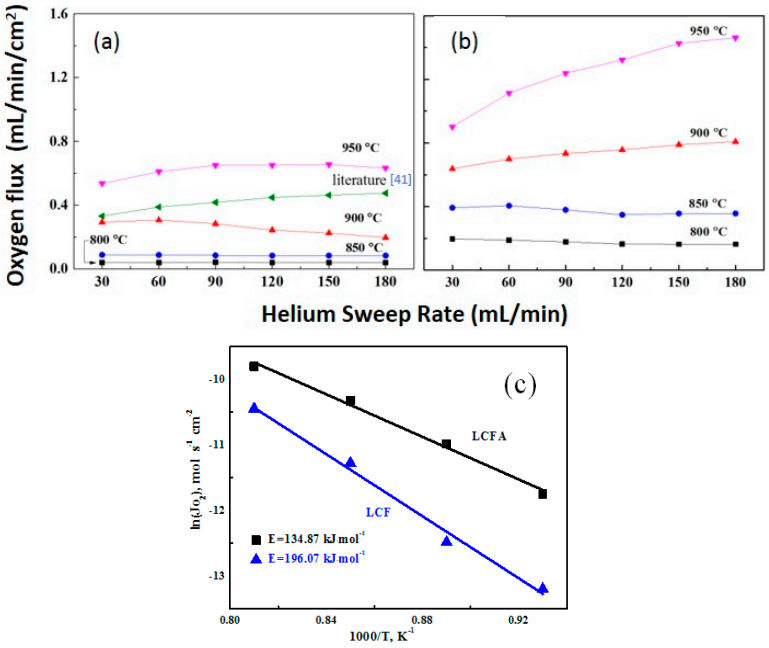

Figure 5. Oxygen fluxes at different operation conditions (**a**) LCF; (**b**) LCFA; and (**c**) Arrhenius plot; air flow rate 100 mL/min.

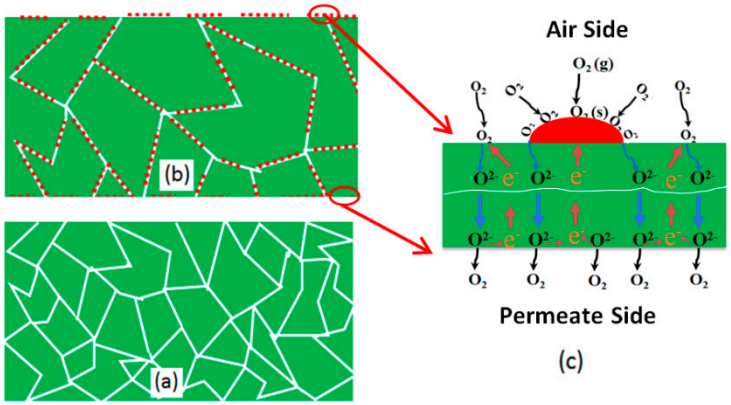

Figure 6. Effects of silver catalyst distribution on the ionic transport through LCF membrane for oxygen permeation (**a**) pure LCF without Ag; (**b**) LCFA; (**c**) inset showing the oxygen permeation behavior. Green area: LCF; red dots: Ag particles; and white lines: grain boundary area of the sintered LCF particles.

Oxygen permeation through a mixed ionic–electronic conducting membrane from the high oxygen partial pressure air side to the low oxygen partial pressure (permeate) side includes the following five steps.

(1) Surface adsorption: Mass transfer of gaseous oxygen from the feed gas to be adsorbed on the membrane surface (air side) (Figure 6c).

(2) Surface reaction: The surface (air side) reactions for oxygen reduction reaction (ORR) occur as below,

$$\frac{1}{2}o_2 + 2e + V_o^{\cdot\cdot} \rightarrow O_o^x \ (ORR)$$

where o_o^x, $V_o^{\cdot\cdot}$ and e stand for lattice oxygen, oxygen vacancy and electron, respectively.

(3) Bulk diffusion: Oxygen ion (or oxygen vacancy) diffusion across the bulk membrane. Oxygen ions diffuse from surface air side to bulk side and further to the permeate side, which is also equivalent to the diffusion of oxygen vacancy in the opposite direction. Noteworthy is that electron diffuses through the membrane from permeate to the air side.

(4) Surface reaction: Lattice oxygen is oxidized to molecular oxygen and electron has been released at the membrane surface (permeate side) during the oxygen escape reaction (OER) process.

$$o_o^x \rightarrow \frac{1}{2}o_2 + 2e + V_o^{\cdot\cdot} \ (OER)$$

(5) Surface desorption: Mass transfer of oxygen from the membrane surface to the sweep gas.

Previous results indicated that in the perovskite oxide membranes with the thickness less than 1 mm, the overall oxygen permeation process is jointly controlled by the surface exchange reactions and ionic bulk diffusion [37,60]. This is just the case for the prepared LCF hollow fiber membrane (Figure 6a) in this work. Thus, Ag catalyst deposition (Figure 6b) on the membrane surface will promote the mass transport at step-1 and step-5 through the spillover effect as shown in Figure 6c. Via the Ag particles, oxygen molecules in the air were more easily adsorbed and dissociated into oxygen ions in step-1 and vice visa in step-5 [62].

Conventionally, the silver particles coated on the membrane surface via dip-coating or the brush-painting methods are usually in an irregular agglomerated state. Another disadvantage associated with such conventional coating is the accelerated Ag aggregation during the high-temperature operation due to the low melting point of Ag (around 960 °C) as observed previously [46]. The introduction of Ag inside the LCF (Figure 6b) was started by adding the four metal ions of La, Ca, Fe, and Ag in the complexation solution, achieving a uniform mixing at the molecular level. During the subsequent organic burning out under oxygen-containing atmosphere, some intermediates will be produced like carbon or CO, which could immediately reduce Ag^+ to Ag. During subsequent high-temperature (1250 °C) sintering process to form perovskite oxide membranes, Ag would exist as the impurity phase inside the bulk LCF along the grain boundary area. Due to the lower melting point of Ag, it plays the sintering aid to facilitate the LCF densification. Consistent with this analysis, the average grain size of LCFA is much larger than LCF as observed in Figure 3e,f. Part of the formed Ag exposed on membrane surface will play the catalyst to boost the oxygen exchange reactions.

3.4. Oxygen Permeation Performance under CO_2 Atmosphere

From industrial applications, the CO_2-containing atmosphere is unavoidable for these perovskite oxide membranes; for example, even the feed gas–air has the trace content of CO_2, thus understanding the permeation stability under CO_2 atmosphere is important. For this purpose, oxygen permeation flux of another LCFA hollow fiber membrane at 900 °C swept by different gases in sequence with pure He, the mixture of 50% He + 50% CO_2, and pure CO_2 was investigated at 900 °C for 900 min with results presented in Figure 7a. Initially, under pure helium, the oxygen flux was 0.65 mL min^{-1} cm^{-2}. When the sweep gas was switched from pure He to 50% CO_2 + He, the oxygen flux was reduced to 0.54 mL min^{-1} cm^{-2}. Swept by pure CO_2 atmosphere, the flux was further decreased to 0.52 mL min^{-1} cm^{-2} for 100% CO_2 atmosphere. This flux decay is mainly due to the strong surface adsorption of CO_2 occupying the membrane surface oxygen vacancies, inhibiting surface oxygen desorption process [39]. Despite the minor flux decrease in CO_2 atmosphere, the encouraging result is the good stability. Irrespective of the sweep gas containing 50% or 100% CO_2, the oxygen flux was very stable.

By contrast, the cobalt-containing perovskite oxide membrane of $Ba_{0.5}Sr_{0.5}Co_{0.8}Fe_{0.2}O_{3-\delta}$ (BSCF) is featured by much higher fluxes under gas atmosphere without CO_2; however, once pure CO_2 was introduced, the flux of BSCF was immediately decreased to zero as shown in Figure 7a (the inset) from our previous result [41]. High stability against acid gases like CO_2 at high temperatures will expand the applications of these LCFA perovskite oxide membranes for clean energy related projects like Oxyfuel combustion for CO_2 capture in power plants. Figure 7b,c shows the TEM and EDS spectra of the tested LCFA hollow fiber membrane. As can be seen, after the long term permeation test, the five elements of LCFA, in particular Ag, are still present, which confirms the membrane stability.

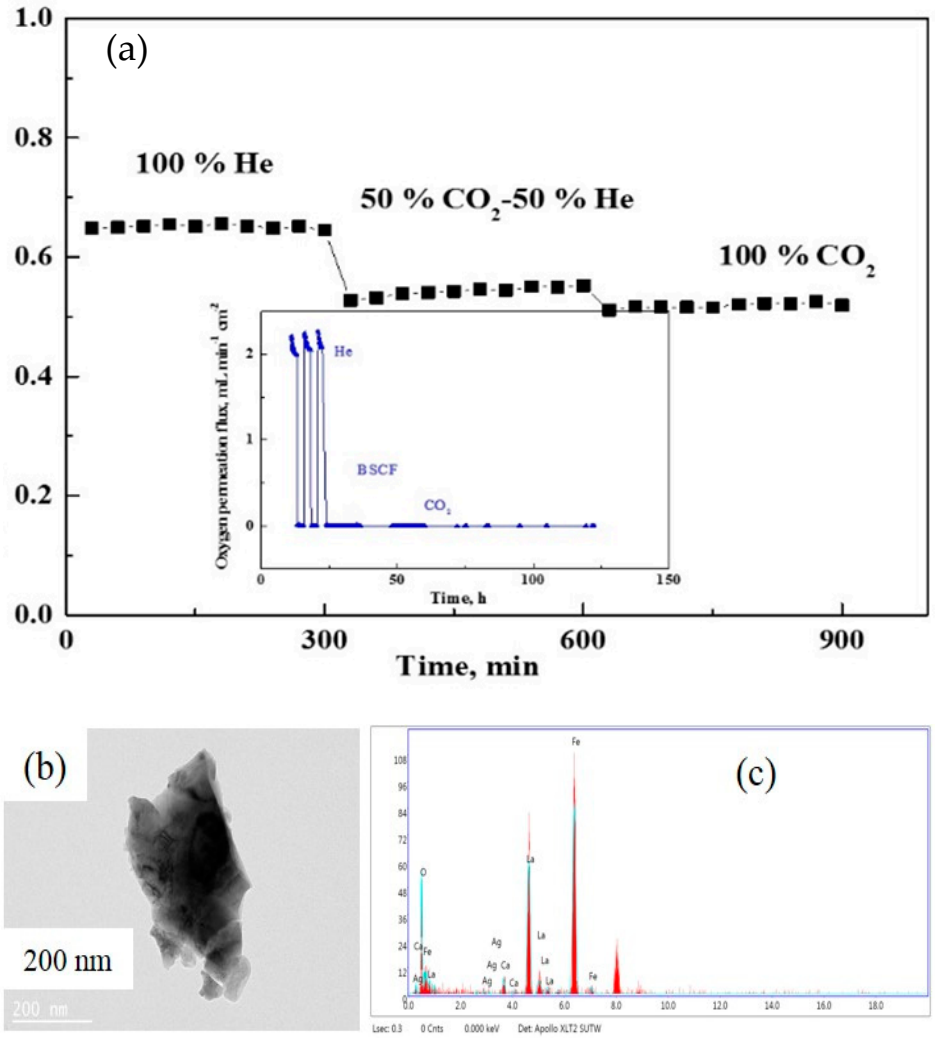

Figure 7. Oxygen permeation stability test (**a**) (flux versus permeation time) of LCFA hollow fiber membrane (operation temperature at 900 °C swept by 100% He, 50% He + 50% CO_2, and 100% CO_2 for 900 min; sweep gas flow rate: 100 mL min^{-1}). (Inset: previous result of $Ba_{0.5}Sr_{0.5}Co_{0.8}Fe_{0.2}O_{3-\delta}$ membrane swept by 100% He and 100% CO_2 [41]) and typical TEM (**b**) and EDS spectra (**c**) of the LCFA powder crushed from LCFA hollow fiber membrane after permeation test.

4. Conclusions

Silver (Ag) as the catalyst can be used to modify the perovskite oxide hollow fiber membranes for oxygen separation. The method of Ag particle distribution has a significant influence on the oxygen permeation behavior. This work comparatively studied the effect of Ag incorporation via a uniform distribution starting from the powder synthesis to be used as the membrane material and a conventional membrane surface coating method. $La_{0.8}Ca_{0.2}Fe_{0.94}O_{3-a}$ + 0.05Ag (LCFA) membrane

prepared from the wet complexion method from nitrate salts displayed remarkably higher oxygen permeation fluxes over the membranes of pure $La_{0.8}Ca_{0.2}Fe_{0.94}O_{3-a}$ (LCF). Operated at 950 °C under the sweep gas mode, the best oxygen flux values of LCF and LCFA hollow fiber membranes were 0.65 and 1.46 mL cm^{-2} min^{-1}, respectively. The incorporation of Ag starting from powder synthesis using one-pot method is more effective to promote the oxygen permeation as the incorporated Ag (around 2.4% by weight) not only works as the catalyst but also as the sintering aid to increase the grain size of LCF membrane sintered at higher temperatures.

Author Contributions: S.L. conceived and designed the experiments; T.M. performed the experiments; N.H., B.M. and S.L. analyzed the data; B.M. and N.Y. contributed reagents/materials/analysis tools; N.H. and S.L. wrote the paper, and Z.Z. helped to revise the manuscript.

Acknowledgments: The research was funded by the Australian Research Council Discovery Project Program, grant number: DP160104937.

Conflicts of Interest: The authors declare no conflict of interest.

References

1. Liu, N.; Tan, X.; Meng, B.; Liu, S. Honeycomb-structured perovskite hollow fibre membranes with ultra-thin densified layer for oxygen separation. *Sep. Purif. Technol.* **2011**, *80*, 396–401. [CrossRef]
2. Liu, Y.; Zhu, X.; Li, M.; O'Hayre, R.P.; Yang, W. Nanoparticles at grain boundaries inhibit the phase transformation of perovskite membrane. *Nano Lett.* **2015**, *15*, 7678–7683. [CrossRef]
3. Wei, Y.; Liao, Q.; Li, Z.; Wang, H. Enhancement of oxygen permeation through U-shaped K_2NiF_4-type oxide hollow fiber membranes by surface modifications. *Sep. Purif. Technol.* **2013**, *110*, 74–80. [CrossRef]
4. Zhu, J.; Liu, G.; Liu, Z.; Chu, Z.; Jin, W.; Xu, N. Unprecedented perovskite oxyfluoride membranes with high-efficiency oxygen ion transport paths for low-temperature oxygen permeation. *Adv. Mater.* **2016**, *28*, 3511–3515. [CrossRef]
5. Wang, H.; Tablet, C.; Caro, J. Oxygen production at low temperature using dense perovskite hollow fiber membranes. *J. Membr. Sci.* **2008**, *322*, 214–217. [CrossRef]
6. Han, N.; Wei, Q.; Tian, H.; Zhang, S.; Zhu, Z.; Liu, J.; Liu, S. Highly stable dual-phase membrane based on $Ce_{0.9}Gd_{0.1}O_{2-\delta}$-$La_2NiO_{4+\delta}$ for oxygen permeation under pure CO_2 atmosphere. *Energy Technol.* **2018**. [CrossRef]
7. Chen, C.-S.; Ran, S.; Liu, W.; Yang, P.; Peng, D.; Bouwmeester, H.J.M. $YBa_2Cu_3O_{6+\delta}$ as an oxygen separation membrane. *Angew. Chem. Int. Ed.* **2001**, *40*, 784–786. [CrossRef]
8. Yoon, K.J.; Marina, O.A. Highly stable dual-phase $Y_{0.8}Ca_{0.2}Cr_{0.8}Co_{0.2}O_3$-$Sm_{0.2}Ce_{0.8}O_{1.9}$ ceramic composite membrane for oxygen separation. *J. Membr. Sci.* **2016**, *499*, 301–306. [CrossRef]
9. Shao, X.; Dong, D.; Parkinson, G.; Li, C.-Z. Improvement of oxygen permeation through microchanneled ceramic membranes. *J. Membr. Sci.* **2014**, *454*, 444–450. [CrossRef]
10. Sunarso, J.; Baumann, S.; Serra, J.M.; Meulenberg, W.A.; Liu, S.; Lin, Y.; Diniz da Costa, J.C. Mixed ionic-electronic conducting ceramic-based membranes for oxygen separation. *J. Membr. Sci.* **2008**, *320*, 13–41. [CrossRef]
11. Li, K.; Tan, X.; Liu, Y. Single-step fabrication of ceramic hollow fibers for oxygen permeation. *J. Membr. Sci.* **2006**, *272*, 1–5. [CrossRef]
12. Tan, X.; Liu, N.; Meng, B.; Liu, S. Morphology control of the perovskite hollow fibre membranes for oxygen separation using different bore fluids. *J. Membr. Sci.* **2011**, *378*, 308–318. [CrossRef]
13. An, R.; Song, J.; Li, Y.; Tan, X.; Sunarso, J.; Zhang, C.; Wang, S.; Liu, S. Bundling strategy to simultaneously improve the mechanical strength and oxygen permeation flux of the individual perovskite hollow fiber membranes. *J. Membr. Sci.* **2017**, *527*, 137–142. [CrossRef]
14. Zhu, J.; Zhang, G.; Liu, G.; Liu, Z.; Jin, W.; Xu, N. Perovskite Hollow Fibers with Precisely Controlled Cation Stoichiometry via One-Step Thermal Processing. *Adv. Mater.* **2017**, *29*, 1606377. [CrossRef] [PubMed]
15. Leo, A.; Motuzas, J.; Yacou, C.; Liu, S.; Serra, J.; Navarrete, L.; Drennan, J.; Julbe, A.; Diniz da Costa, J.C. Copper oxide-perovskite mixed matrix membranes delivering very high oxygen fluxes. *J. Membr. Sci.* **2017**, *526*, 323–333. [CrossRef]

16. Jin, W.; Li, S.; Huang, P.; Xu, N.; Shi, J.; Lin, Y.S. Tubular lanthanum cobaltite perovskite-type membrane reactors for partial oxidation of methane to syngas. *J. Membr. Sci.* **2000**, *66*, 13–22. [CrossRef]
17. Zhuang, S.; Han, N.; Wang, T.; Meng, X.; Meng, B.; Li, Y.; Sunarso, J.; Liu, S. Enhanced CO selectivity for reverse water-gas shift reaction using Ti_4O_7-doped $SrCe_{0.9}Y_{0.1}O_{3-\delta}$ hollow fiber membrane reactor. *Can. J. Chem. Eng.* **2018**, *9999*, 1–8. [CrossRef]
18. Czyperek, M.; Zapp, P.; Bouwmeester, H.J.M.; Modigell, M.; Ebert, K.; Voigt, I.; Meulenberg, W.A.; Singheiser, L.; Stöver, D. Gas separation membranes for zero-emission fossil power plants: MEM-BRAIN. *J. Membr. Sci.* **2010**, *359*, 149–159. [CrossRef]
19. Pei, S.; Kleefisch, M.S.; Kobylinski, T.P.; Faber, J.; Udovich, C.A.; Zhang-McCoy, V.; Dabrowski, B.; Balachandran, U.; Mieville, R.L.; Poeppel, R.B. Failure mechanisms of ceramic membrane reactors in partial oxidation of methane to synthesis gas. *Catal. Lett.* **1995**, *30*, 201–212. [CrossRef]
20. Kneer, R.; Toporov, D.; Förster, M.; Christ, D.; Broeckmann, C.; Pfaff, E.; Zwick, M.; Engels, S.; Modigell, M. OXYCOAL-AC: Towards an integrated coal-fired power plant process with ion transportmembrane-based oxygen supply. *Energy Environ. Sci.* **2010**, *3*, 198–207. [CrossRef]
21. Waindich, A.; Möbius, A.; Müller, M. Corrosion of $Ba_{1-x}Sr_xCo_{1-y}Fe_yO_{3-\delta}$ and $La_{0.3}Ba_{0.7}Co_{0.2}Fe_{0.8}O_{3-\delta}$ materials for oxygen separating membranes under Oxycoal conditions. *J. Membr. Sci.* **2009**, *337*, 182–187. [CrossRef]
22. Zhu, J.; Guo, S.; Chu, Z.; Jin, W. Effects of polymer binders on separation performance of the perovskite-type 4-bore hollow fiber membranes. *Sep. Purif. Technol.* **2017**, *187*, 294–302.
23. Lin, Y.S.; Wang, W.; Han, J. Oxygen permeation through thin mixed-conducting solid oxide membranes. *AIChE J.* **1994**, *40*, 786–798. [CrossRef]
24. Li, H.; Liu, Y.; Zhu, X.; Cong, Y.; Xu, S.; Xu, W.; Yang, W. Oxygen permeation through Ca-contained dual-phase membranes for oxyfuel CO_2 capture. *Sep. Purif. Technol.* **2013**, *114*, 31–37. [CrossRef]
25. Tan, X.; Shi, L.; Hao, G.; Meng, B.; Liu, S. $La_{0.7}Sr_{0.3}FeO_{3-\delta}$ perovskite hollow fiber membranes for oxygen permeation and methane conversion. *Sep. Purif. Technol.* **2012**, *96*, 89–97. [CrossRef]
26. Engels, S.; Markus, T.; Modigell, M.; Singheiser, L. Oxygen permeation and stability investigations on MIEC membrane materials under operating conditions for power plant processes. *J. Membr. Sci.* **2011**, *370*, 58–69. [CrossRef]
27. Gao, J.; Lun, Y.; Han, N.; Tan, X.; Fan, C.; Liu, S. Influence of nitric oxide on the oxygen permeation behavior of $La_{0.6}Sr_{0.4}Co_{0.2}Fe_{0.8}O_{3-\delta}$ perovskite membranes. *Sep. Purif. Technol.* **2019**, *210*, 900–906. [CrossRef]
28. Efimov, K.; Klande, T.; Juditzki, N.; Feldhoff, A. Ca-containing CO_2-tolerant perovskite materials for oxygen separation. *J. Membr. Sci.* **2012**, *389*, 205–215. [CrossRef]
29. Zhang, K.; Shao, Z.; Li, C.; Liu, S. Novel CO_2-tolerant ion-transporting ceramic membranes with an external short circuit for oxygen separation at intermediate temperatures. *Energy Environ. Sci.* **2012**, *5*, 5257–5264. [CrossRef]
30. Fang, W.; Steinbach, F.; Chen, C.; Feldhoff, A. An approach to enhance the CO_2 tolerance of fluorite-perovskite dual-phase oxygen-transporting membrane. *Chem. Mater.* **2015**, *27*, 7820–7826. [CrossRef]
31. Yang, D.; Han, N.; Han, D.; Meng, B.; Wang, G.; Liu, S. Novel $SrCo_{0.9}W_{0.1}O_{3-\delta}$ hollow fiber membrane with enhanced oxygen delivery performance and CO_2 resistance ability. *Chem. Sel.* **2018**, *3*, 13700–13704.
32. Li, Q.; Zhu, X.; He, Y.; Yang, W. Oxygen permeability and stability of $BaCe_{0.1}Co_{0.4}Fe_{0.5}O_{3-\delta}$ oxygen permeable membrane. *Sep. Purif. Technol.* **2010**, *73*, 38–43. [CrossRef]
33. Han, N.; Zhang, S.; Meng, X.; Yang, N.; Meng, B.; Tan, X.; Liu, S. Effect of enhanced oxygen reduction activity on oxygen permeation of $La_{0.6}Sr_{0.4}Co_{0.2}Fe_{0.8}O_{3-\delta}$ membrane decorated by K_2NiF_4-type oxide. *J. Alloys Compd.* **2016**, *654*, 280–289. [CrossRef]
34. Chen, X.; Huang, L.; Wei, Y.; Wang, H. Tantalum stabilized $SrCoO_{3-\delta}$ perovskite membrane for oxygen separation. *J. Membr. Sci.* **2011**, *368*, 159–164. [CrossRef]
35. Zhang, G.; Liu, Z.; Zhu, N.; Jiang, W.; Dong, X.; Jin, W. A novel Nb_2O_5-doped $SrCo_{0.8}Fe_{0.2}O_{3-\delta}$ oxide with high permeability and stability for oxygen separation. *J. Membr. Sci.* **2012**, *405*, 300–309. [CrossRef]
36. Ran, R.; Guo, Y.; Gao, D.; Liu, S.; Shao, Z. Effect of foreign oxides on the phase structure, sintering and transport properties of $Ba_{0.5}Sr_{0.5}Co_{0.8}Fe_{0.2}O_{3-\delta}$ as ceramic membranes for oxygen separation. *Sep. Purif. Technol.* **2011**, *81*, 384–391. [CrossRef]
37. Zeng, P.; Ran, R.; Chen, Z.; Gu, H.; Shao, Z.; Liu, S. Novel mixed conducting $SrSc_{0.05}Co_{0.95}O_{3-\delta}$ ceramic membrane for oxygen separation. *AICHE J.* **2007**, *53*, 3116–3124. [CrossRef]

38. He, B.; Ding, D.; Ling, Y.; Xu, J.; Zhao, L. Efficient modification for enhancing surface activity of $Ba_{0.5}Sr_{0.5}Co_{0.8}Fe_{0.2}O_{3-\delta}$ oxygen permeation membrane. *J. Membr. Sci.* **2015**, *477*, 7–13. [CrossRef]
39. Tan, X.; Liu, N.; Meng, B.; Sunarso, J.; Zhang, K.; Liu, S. Oxygen permeation behavior of $La_{0.6}Sr_{0.4}Co_{0.2}Fe_{0.8}O_{3-\delta}$ hollow fibre membranes with highly concentrated CO_2 exposure. *J. Membr. Sci.* **2012**, *389*, 216–222. [CrossRef]
40. Zhang, C.; Sunarso, J.; Liu, S. Designing CO_2-resistant oxygen-selective mixed ionic-electronic conducting membranes: Guidelines, recent advances and future directions. *Chem. Soc. Rev.* **2017**, *46*, 2941–3005. [CrossRef]
41. Yang, D.; Yang, N.; Meng, B.; Tan, X.; Zhang, C.; Sunarso, J.; Zhu, Z.; Liu, S. A-Site Excess $(La_{0.8}Ca_{0.2})_{1.01}FeO_{3-\delta}$ (LCF) Perovskite Hollow Fiber Membrane for Oxygen Permeation in CO_2-Containing Atmosphere. *Energy Fuels* **2017**, *31*, 4531–4538. [CrossRef]
42. Zhu, X.; Cong, Y.; Yang, W. Oxygen permeability and structural stability of $BaCe_{0.15}Fe_{0.85}O_{3-\delta}$ membranes. *J. Membr. Sci.* **2006**, *283*, 38–44. [CrossRef]
43. Price, P.M.; Butt, D.P. Stability and Decomposition of Ca-Substituted Lanthanum Ferrite in Reducing Atmospheres. *J. Am. Ceram. Soc.* **2015**, *98*, 2881–2886. [CrossRef]
44. Leo, A.; Smart, S.; Liu, S.; Diniz da Costa, J.C. High Performance Perovskite Hollow Fibres for Oxygen Separation. *J. Membr. Sci.* **2011**, *368*, 64–68. [CrossRef]
45. Leo, A.; Liu, S.; Diniz da Costa, J.C.; Shao, Z. Oxygen permeation through perovskite membranes and the improvement of oxygen flux by surface modification. *Sci. Technol. Adv. Mater.* **2007**, *7*, 819–825. [CrossRef]
46. Tan, X.; Wang, Z.; Liu, H.; Liu, S. Enhancement of oxygen permeation through $La_{0.6}Sr_{0.4}Co_{0.2}Fe_{0.8}O_{3-\delta}$ hollow fiber membranes by surface modifications. *J. Membr. Sci.* **2008**, *324*, 128–135. [CrossRef]
47. Savinskaya, O.A.; Nemudry, A.P. Oxygen permeability and structural features of $SrFe_{1-x}W_xO_{3-\delta}$ membranes. *J. Membr. Sci.* **2014**, *459*, 45–51. [CrossRef]
48. Ovalle-Encinia, O.; Pfeiffer, H.; Ortiz-Landeros, J. CO_2 Separation improvement produced on a ceramic–carbonate dense membrane superficially modified with Au–Pd. *Ind. Eng. Chem. Res.* **2018**, *57*, 9261–9268. [CrossRef]
49. Chu, Y.; Tan, X.; Shen, Z.; Liu, P.; Han, N.; Kang, J.; Duan, X.; Wang, S.; Liu, L.; Liu, S. Efficient removal of organic and bacterial pollutants by Ag-$La_{0.8}Ca_{0.2}Fe_{0.94}O_{3-\delta}$ perovskite via catalytic peroxymonosulfate activation. *J. Hazard. Mater.* **2018**, *356*, 53–60. [CrossRef]
50. Tan, X.; Liu, Y.; Li, K. Preparation of LSCF ceramic hollow-fiber membranes for oxygen production by a phase-inversion/sintering technique. *Ind. Eng. Chem. Res.* **2005**, *44*, 61–66. [CrossRef]
51. Han, N.; Zhang, S.; Meng, B.; Tan, X. The effect of microstructure and surface decoration with K_2NiF_4-type oxide upon the oxygen permeability of perovskite-type $La_{0.7}Sr_{0.3}FeO_{3-\delta}$ hollow fiber membranes. *RSC Adv.* **2015**, *5*, 88602–88611. [CrossRef]
52. Tan, X.; Liu, Y.; Li, K. Mixed conducting ceramic hollow-fiber membranes for air separation. *AIChE J.* **2005**, *51*, 1991–2000. [CrossRef]
53. Han, N.; Meng, B.; Yang, N.; Sunarso, J.; Zhu, Z.; Liu, S. Enhancement of oxygen permeation fluxes of $La_{0.6}Sr_{0.4}CoO_{3-\delta}$ hollow fiber membrane via macrostructure modification and $(La_{0.5}Sr_{0.5})_2CoO_{4+\delta}$ decoration. *Chem. Eng. Res. Des.* **2018**, *134*, 487–496. [CrossRef]
54. Wang, H.; Tablet, C.; Yang, W.; Caro, J. In situ high temperature X-ray diffraction studies of mixed ionic and electronic conducting perovskite-type membranes. *Mater. Lett.* **2005**, *59*, 3750–3755. [CrossRef]
55. Zhou, W.; Ran, R.; Shao, Z.; Jin, W.; Xu, N. Evaluation of A-site cation-deficient $(Ba_{0.5}Sr_{0.5})_{1-x}Co_{0.8}Fe_{0.2}O_{3-\delta}$ ($x > 0$) perovskite as a solid-oxide fuel cell cathode. *J. Power Sources* **2008**, *182*, 24–31. [CrossRef]
56. Zhang, Z.; Chen, Y.; Tade, M.O.; Hao, Y.; Liu, S.; Shao, Z. Tin-doped perovskite mixed conducting membrane for efficient air separation. *J. Mater. Chem. A* **2014**, *2*, 9666–9674. [CrossRef]
57. Tan, X.; Liu, S.; Li, K. Preparation and characterization of inorganic hollow fiber membranes. *J. Membr. Sci.* **2001**, *188*, 87–95. [CrossRef]
58. Zeng, P.; Ran, R.; Chen, Z.; Gu, H.; Shao, Z.; Diniz da Costa, J.C.; Liu, S. Significant effects of sintering temperature on the performance of $La_{0.6}Sr_{0.4}Co_{0.2}Fe_{0.8}O_{3-\delta}$ oxygen selective membranes. *J. Membr. Sci.* **2007**, *302*, 171–179. [CrossRef]
59. Liu, S.; Tan, X.; Li, K.; Hughes, R. Preparation and characterisation of $SrCe_{0.95}Yb_{0.05}O_{2.975}$ hollow fibre membranes. *J. Membr. Sci.* **2001**, *193*, 249–260. [CrossRef]

60. Ge, L.; Shao, Z.; Zhang, K.; Ran, R.; Diniz da Costa, J.C.; Liu, S. Evaluation of mixed-conducting lanthanum-strontium-cobaltite ceramic membrane for oxygen separation. *AIChE J.* **2009**, *55*, 2603–2613. [CrossRef]
61. Zhu, X.; Liu, H.; Cong, Y.; Yang, W. Permeation model and experimental investigation of mixed conducting membranes. *AIChE J.* **2012**, *58*, 1744–1754. [CrossRef]
62. Leo, A.; Liu, S.; Diniz da Costa, J.C. The enhancement of oxygen flux on $Ba_{0.5}Sr_{0.5}Co_{0.8}Fe_{0.2}O_{3-\delta}$ (BSCF) hollow fibers using silver surface modification. *J. Membr. Sci.* **2009**, *340*, 148–153. [CrossRef]